

Orbitally-paced climate evolution during the middle Miocene “Monterey” carbon-isotope excursion

Ann Holbourn^{a,*}, Wolfgang Kuhnt^a, Michael Schulz^b,
José-Abel Flores^c, Nils Andersen^d

^a *Institute of Geosciences, Christian-Albrechts-University, D-24118 Kiel, Germany*

^b *Department of Geosciences and DFG-Research Center “Ocean Margins”, University of Bremen, D-28334 Bremen, Germany*

^c *Department of Geology, University of Salamanca, 37008 Salamanca, Spain*

^d *Leibniz Laboratory for Radiometric Dating and Stable Isotope Research, Christian-Albrechts-University, D-24118 Kiel, Germany*

Received 31 January 2007; received in revised form 9 July 2007; accepted 11 July 2007

Available online 24 July 2007

Editor: M.L. Delaney

Abstract

One of the most enigmatic features of Cenozoic long-term climate evolution is the long-lasting positive carbon-isotope excursion or “Monterey Excursion”, which started during a period of global warmth after 16.9 Ma and ended at ~13.5 Ma, approximately 400 kyr after major expansion of the Antarctic ice-sheet. We present high-resolution (1–9 kyr) astronomically-tuned climate proxy records in two complete sedimentary successions from the northwestern and southeastern Pacific (ODP Sites 1146 and 1237), which shed new light on the middle Miocene carbon-isotope excursion and associated climatic transition over the interval 17.1–12.7 Ma. We recognize three distinct climate phases with different imprints of orbital variations into the climatic signals (1146 and 1237 $\delta^{18}\text{O}$, $\delta^{13}\text{C}$; 1237 XRF Fe, fraction >63 μm): (1) climate optimum prior to 14.7 Ma characterized by minimum ice volume and prominent 100 and 400 kyr variability, (2) long-term cooling from 14.7 to 13.9 Ma, principally driven by obliquity and culminating with rapid cryosphere expansion and global cooling at the onset of the last and most pronounced $\delta^{13}\text{C}$ increase, (3) “Icehouse” mode after 13.9 Ma with distinct 100 kyr variability and improved ventilation of the deep Pacific. The “Monterey” carbon-isotope excursion (16.9–13.5 Ma) consists overall of nine 400 kyr cycles, which show high coherence with the long eccentricity period. Superposed on these low-frequency oscillations are high-frequency variations (100 kyr), which closely track the amplitude modulation of the short eccentricity period. In contrast to $\delta^{13}\text{C}$, the $\delta^{18}\text{O}$ signal additionally shows significant power in the 41 kyr band, and the 1.2 Myr amplitude modulation of the obliquity cycle is clearly imprinted in the 1146 $\delta^{18}\text{O}$ signal. Our results suggest that eccentricity was a prime pacemaker of middle Miocene climate evolution through the modulation of long-term carbon budgets and that obliquity-paced changes in high-latitude seasonality favored the transition into the “Icehouse” climate.

© 2007 Elsevier B.V. All rights reserved.

Keywords: middle Miocene; Monterey Excursion; stable isotopes; cyclostratigraphy; ODP Site 1146; ODP Site 1237

1. Introduction

The middle Miocene climatic transition, which began with an extended period of global warmth and ended with the development of permanent ice sheets in Antarctica,

* Corresponding author.

E-mail address: ah@gpi.uni-kiel.de (A. Holbourn).

marked one of the four major steps in Cenozoic cooling (Zachos et al., 2001a and references therein). Perhaps the most striking feature of this extraordinary interval in Earth's climate evolution is the long-lasting positive carbon-isotope excursion (the "Monterey Excursion" of Vincent and Berger, 1985), which started close to 16.9 Ma and ended at ~13.5 Ma, approximately 400 kyr after major expansion of the Antarctic ice-sheet. Bulk carbonate as well as planktonic and benthic foraminiferal stable isotope records in oceanic successions initially revealed that this prolonged $\delta^{13}\text{C}$ excursion was characterized by low-frequency fluctuations (~1‰), which appeared to approximate long eccentricity cycles (Woodruff and Savin, 1991). The apparent co-variance between $\delta^{13}\text{C}$ and $\delta^{18}\text{O}$ gave support to the hypothesis that periodic increased burial of organic carbon drove atmospheric CO_2 drawdown, spurring Miocene global cooling (Vincent and Berger, 1985; Woodruff and Savin, 1991; Flower and Kennett, 1993, 1994). However, this notion has not been sustained by recent Miocene atmospheric CO_2 reconstructions, indicating relatively low levels during both periods of inferred global warming and high latitude cooling (Pagani et al., 1999, 2005). Yet, the middle Miocene offers a compelling glimpse into a prolonged, warmer climate phase with much reduced ice-sheets, which ended with drastic global cooling. A better understanding of this interval can undoubtedly provide new insights into the climate dynamics of warm periods and the processes driving climate change, as well as help constrain modeling studies of natural climate variability.

To date, this key interval remains one of the most puzzling episodes in Cenozoic climate history. High-resolution time series spanning this critical climatic transition are still extremely scarce, because sedimentary successions have all too often been strongly affected by carbonate dissolution or burial diagenesis or proven incomplete due to major changes in ocean circulation. A further difficulty resides in the uncertainty in dating and inter-correlating records across basins, because age models for this time interval relied often on sparse biostratigraphic and magnetostratigraphic data that were not directly calibrated to an astronomical timescale. Astronomical tuning through the correlation of cyclic sediments to astronomical target curves, initially allowed the development of a global high-resolution timescale for the late Pleistocene (Imbrie et al., 1984). Following innovations in drilling technology and the improvement of orbital solutions, this technique was successfully applied to older intervals of the Neogene (Hilgen et al., 1995; Shackleton and Crowhurst, 1997; Shackleton et al., 1999; Krijgsman et al., 1999; Hilgen et al., 2000, 2003). These efforts resulted in the astronomically-tuned

Neogene timescale ATNTS2004 (Lourens et al., 2004; updated in Hüsing et al., 2007). However, the interval 14–18 Ma has remained problematic, mainly due to the scarcity of continuous successions and the lack of directly correlatable magnetostratigraphic data for integration into orbitally-derived timescales (Lourens et al., 2004).

Miller et al. (1991) originally proposed a new nomenclature for the Miocene based on the recognition of prominent oxygen isotope events (Mi1-6), while Woodruff and Savin (1991) identified seven carbon-isotope maxima (CM1-7) and seven oxygen isotope events (A–G) in the middle Miocene with potential for global correlations. However, the definition and placement of these data have remained evasive, because most records have relatively low temporal resolution and do not capture orbital frequencies. To date, no standard oxygen isotope chronology of astronomically-tuned marine successions is available for the interval 14–18 Ma. Here, we present high-resolution (1–5 kyr) astronomically-tuned climate proxy records in two continuous sedimentary successions from the northwestern (ODP Site 1146, South China Sea, Fig. 1) and southeastern Pacific (ODP Site 1237 off Peru, Fig. 1) covering the complete interval of the middle Miocene "Monterey" carbon-isotope excursion and associated climatic transition. These new chronologies permit detailed correlation of paleoceanographic events across the subtropical Pacific, and allow reconstruction of the carbon-isotope excursion and associated paleoceanographic and climatic changes in unprecedented resolution.

2. Materials and methods

2.1. Sampling strategy

Our study is based on Miocene marine sediments recovered at ODP Site 1146 (19° 27.40'N, 116° 16.37'E; water depth: 2092 m) and Site 1237 (16°0.421'S, 76°22.685'W; water depth: 3212 m). Detailed site locations, core recovery and lithological descriptions can be found in Wang et al. (2000) and Mix et al. (2003).

Coring with the Extended Core Barrel (XCB) system at Site 1146 recovered a continuous Miocene sequence of carbonate-rich hemipelagic sediments, which grade from unlithified green nannofossil clay in the lower Miocene to light brownish gray foraminifers and nannofossil clay in the upper Miocene (Wang et al., 2000). Foraminifers and nannofossil clays were sampled at ~10 cm intervals (~4 kyr time resolution) in Hole 1146A (463.05–568.47 m below seafloor). We did not follow the shipboard splice, but used mostly samples from Hole 1146A because several tie points of the splice

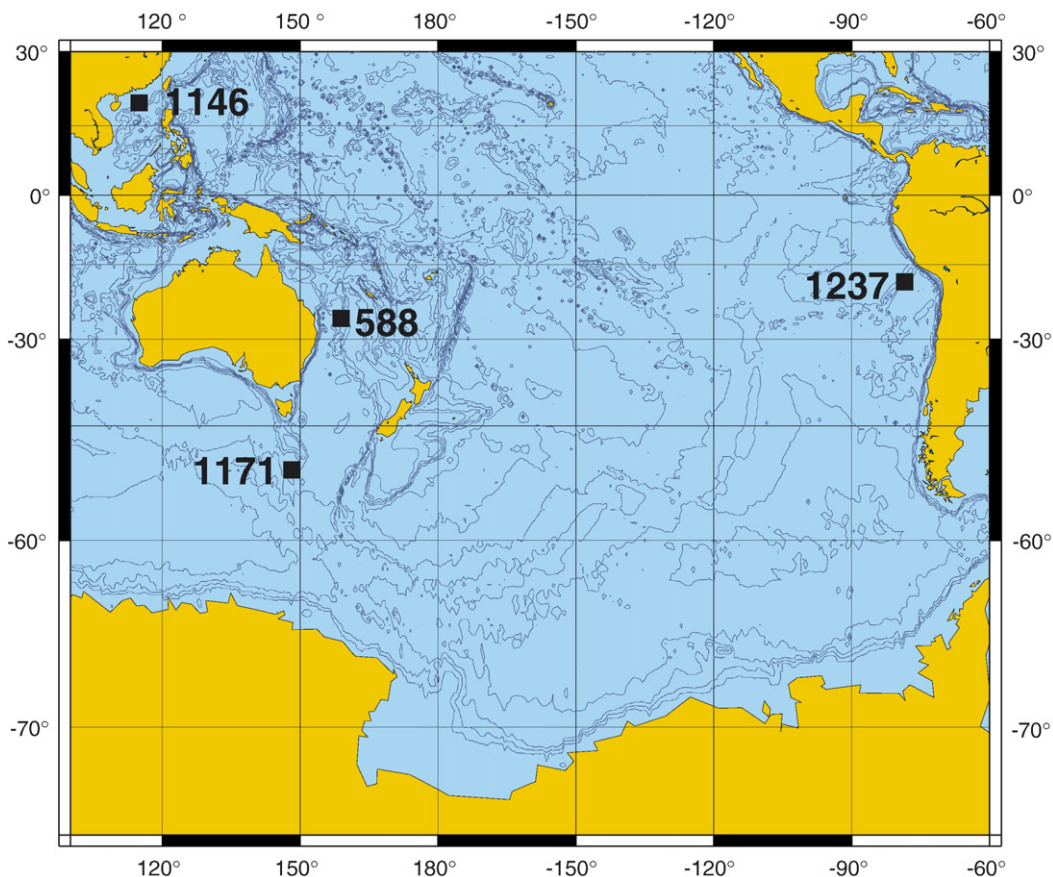


Fig. 1. Location of ODP Site 1146 ($19^{\circ}27.40'N$, $116^{\circ}16.37'E$) drilled at 2092 m water depth in the northern South China Sea, ODP Site 1237 ($16^{\circ}0.421'S$, $76^{\circ}22.685'W$) drilled at 3212 m water depth on the Nazca Ridge, off Peru, DSDP Site 588 ($26^{\circ}06.7'S$, $161^{\circ}13.6'E$) drilled at 1533 m water depth in the South West Pacific and ODP Hole 1171C ($48^{\circ}29.9971'S$, $149^{\circ}6.7051'E$) drilled at 2147.8 m water depth on the southernmost South Tasman Rise.

are ambiguously constrained by the shipboard natural gamma ray, color reflectance and magnetic susceptibility data. Coring gaps between cores ranging between 10 and 40 cm = ~ 4 –16 kyr in Hole 1146A (calculated from core barrel length, stretching factor and measured recovery) were compensated during the tuning process, and four core breaks were resampled in Hole 1146C following the splice with sufficient overlap to verify the completeness of the Hole A record. Oxygen isotope records indicated that the breaks between Cores 1146A-55X and -56X and between Cores 1146A-57X and -58X were minimal and did not require compensation. Two larger coring gaps between Cores 1146A-54X and -55X and Cores 1146A-56X and -57X were bridged with samples from Hole 1146C, based on the match of our isotope records. We consequently shifted the mbsf scale downward by 1 m from the top of Core 1146A-57X (529.9 mbsf). This modified depth scale in Hole 1146A is referred to as mbsf corrected (mbsf corr.).

Middle Miocene sediments recovered with the Advanced Piston Corer (APC) system at Site 1237 consist of unlithified, pale brown nannofossil ooze with an average of 95 wt.% calcium carbonate (Mix et al., 2003). Nannofossil oozes were sampled at ~ 5 cm intervals (~ 4 –9 kyr time resolution) from a composite sequence (shipboard splice) from Holes 1237A and C (189.69–246.76 m composite depth). Overlapping XRF measurements (50–100 cm) were made with 1 cm resolution at correlation points of the Site 1237 splice to verify the completeness of the record.

2.2. Isotope analysis

All samples were oven dried at 40 °C and weighed before washing over a 63 μm sieve. Residues were oven dried at 40 °C on a sheet of filter paper, then weighed and sieved into different size fractions. We measured $\delta^{18}\text{O}$ and $\delta^{13}\text{C}$ in epifaunal benthic foraminifers $>250 \mu\text{m}$

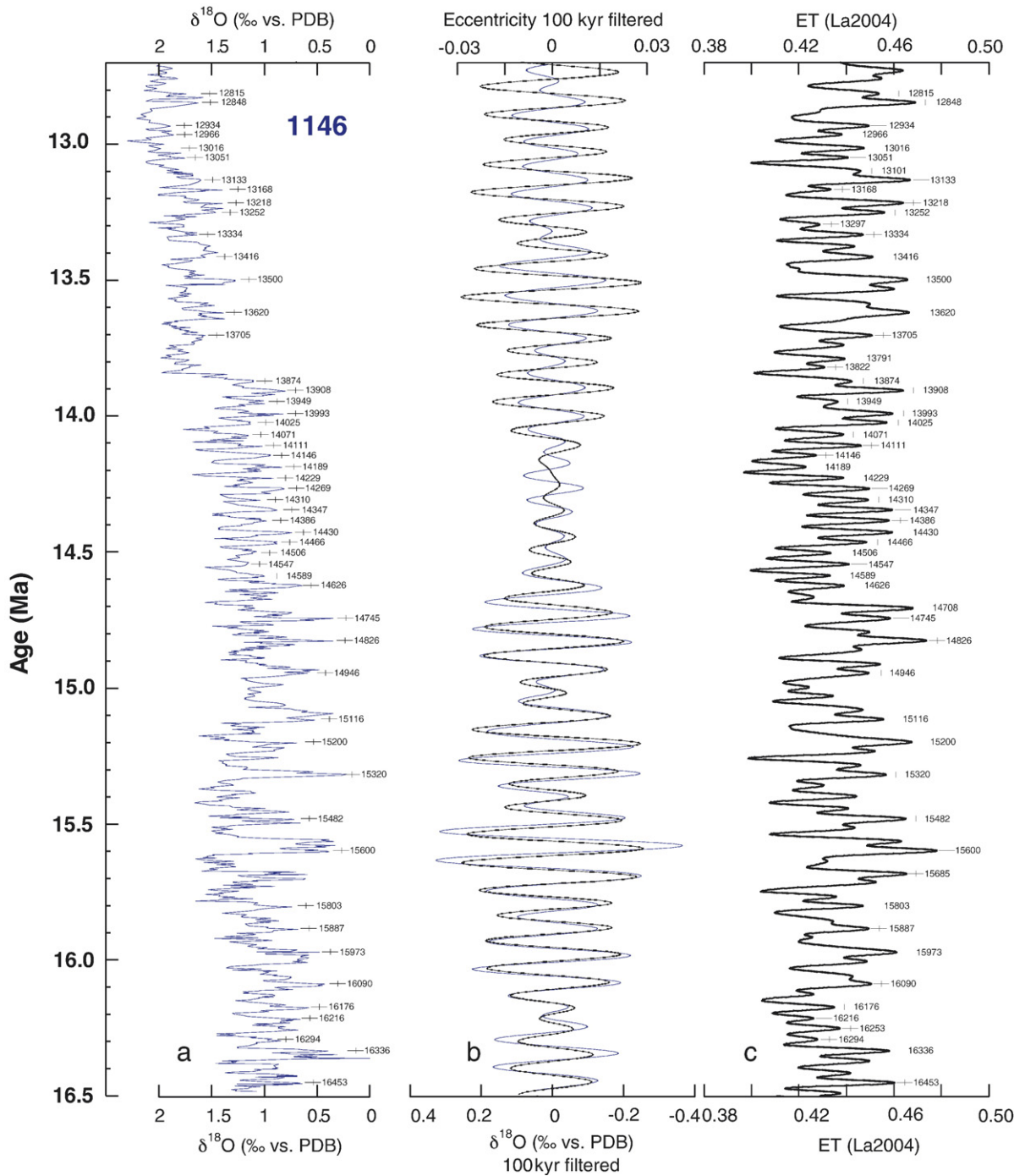


Fig. 2. (a) Benthic foraminiferal $\delta^{18}\text{O}$ profiles in ODP Site 1146, plotted against age (Ma). Age control points (Supplementary Table 3) indicated by crosses (ka). (b) Comparison of 100 kyr filtered $\delta^{18}\text{O}$ (blue) and eccentricity from La2004 (black). Gaussian band-pass filter centered at 0.01 kyr^{-1} (100 kyr period) with 0.003 kyr^{-1} bandwidth (76.9–142.9 kyr period). Note: Filtered $\delta^{18}\text{O}$ record shows similar phasing and amplitude modulation as filtered eccentricity. (c) Eccentricity–tilt tuning target based on La2004. Age correlation points marked by crosses. (For interpretation of the references to colour in this figure legend, the reader is referred to the web version of this article.)

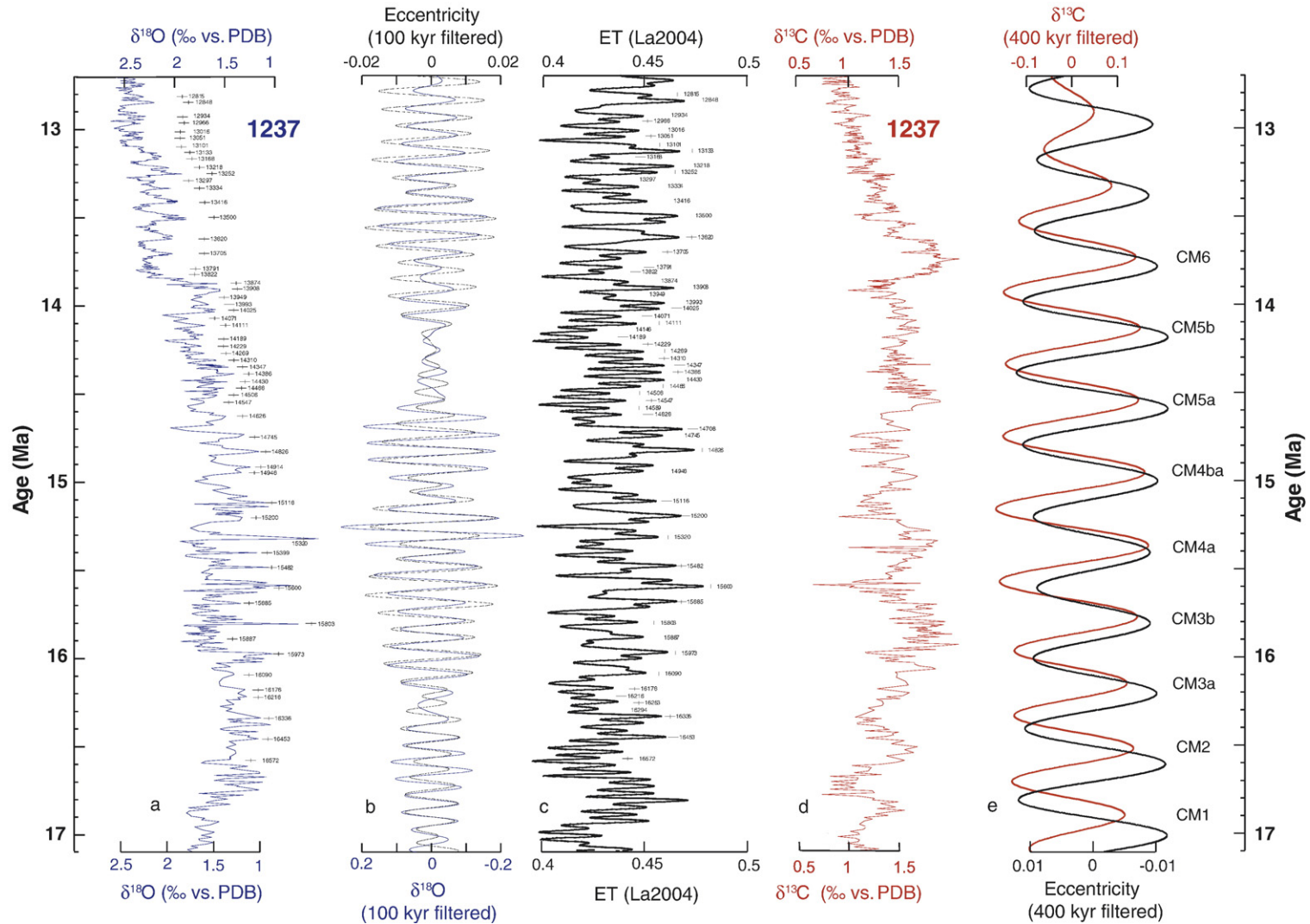


Fig. 3. (a) Benthic foraminiferal $\delta^{18}\text{O}$ profiles in ODP Site 1237, plotted against age (Ma). Age control points (Supplementary Table 3) indicated by crosses (ka). (b) Comparison of 100 kyr filtered $\delta^{18}\text{O}$ (blue) and eccentricity from La2004 (black). Gaussian band-pass filter centered at 0.01 kyr^{-1} (100 kyr period) with 0.003 kyr^{-1} bandwidth (76.9–142.9 kyr period). Note: Filtered $\delta^{18}\text{O}$ record shows similar phasing and amplitude modulation as filtered eccentricity. (c) Eccentricity–tilt tuning target based on La2004. Age correlation points marked by crosses. (d) Benthic foraminiferal $\delta^{13}\text{C}$ in ODP Site 1237. (e) Comparison of 400 kyr filtered $\delta^{13}\text{C}$ (red) and eccentricity from La2004 (black). The “Monterey” carbon-excision consists of nine carbon-isotope maxima. In contrast to the original CM nomenclature in Woodruff and Savin (1991), CM3, CM4 and CM5 consist of two ~ 400 kyr cycles. (For interpretation of the references to colour in this figure legend, the reader is referred to the web version of this article.)

(*Planulina wuellerstorfi* or *Cibicidoides mundulus*, except in ~6% samples in Site 1146, where we analyzed either *Cibicidoides barnetti*, *Cibicidoides bradyi*, *Cibicidoides incrassatus* or *Cibicidoides mexicanus*). Three to ten well-preserved tests were broken into large fragments, cleaned in alcohol in an ultrasonic bath, then dried at 40 °C. In few samples, where foraminiferal density was low, only 1–2 specimens were analyzed. Measurements were made with the Finnigan MAT 251 mass spectrometer at the Leibniz Laboratory, Kiel University. The instrument is coupled on-line to a Carbo-Kiel Device (Type I). Samples were reacted by individual acid addition (99% H₃PO₄ at 73 °C). Standard external error is better than ±0.07‰ and ±0.05‰ for δ¹⁸O and δ¹³C, respectively. Replicate measurements on ~5% of samples indicate mean reproducibility better than ±0.11‰ and ±0.13‰ for δ¹⁸O and δ¹³C, respectively. Paired measurements in 37 samples indicate no significant offset in δ¹⁸O and δ¹³C between *P. wuellerstorfi* and *C. mundulus*. Results were calibrated using the National Institute of Standards and Technology (Gaithersburg, Maryland) carbonate isotope standard NBS 20 and NBS 19 and 18, and are reported on the PeeDee belemnite (PDB) scale. Plots of δ¹⁸O and δ¹³C versus depth are shown in Supplementary Fig. 1. Data sets are archived at WDC-MARE (<http://www.pangaea.de>).

2.3. Chronology

Astronomically-tuned chronologies were developed by correlating the benthic foraminiferal δ¹⁸O record in each site to variations of the Earth's orbit (obliquity and eccentricity in Laskar et al., 2004) and applying a minimal tuning strategy in order to avoid artificial changes in sedimentation rates (Muller and MacDonald, 2000). As tuning target, we used an eccentricity–tilt composite (ET) from Laskar et al. (2004) using the sum of eccentricity and obliquity (in radians), with no phase shift and equal weight of the two components. This tuning target does not include precession, and thus differs from the conventional ETP (Imbrie et al., 1984), which denotes a convenient artificial mix of orbital eccentricity, tilt (obliquity), and precession signals with more or less equal variance (Shackleton, 2000). We did not consider precessional variability in our tuning target, since (1) our isotope records did not display significant variance in the precessional bandwidth, (2) the precise evolution of the precession constant due to tidal dissipation and dynamical ellipticity is still unclear (Laskar, 1999) and (3) we wanted to avoid the potential problem of inconstant phase response to the hemispherically asymmetric precession insolation forcing (Clemens, 1999).

We tuned δ¹⁸O minima to ET maxima, since we assume (1) that relatively warm summers in Antarctica during periods of high obliquity would result in ice sheet melting, whereas cool summers during periods of low obliquity would favor ice sheet growth, and (2) that high obliquity corresponding to low summer insolation gradient between low and high latitudes would decrease poleward moisture transport and reduce ice-sheet build-up (Raymo and Nisancioglu, 2003). We did not adjust our tuning for possible phase lags between δ¹⁸O and obliquity insolation forcing (i.e. 7.8 kyr for the response time of Plio–Pleistocene ice sheets in Shackleton et al., 1995; Clemens, 1999) since the response time of a smaller middle Miocene East Antarctic ice sheet is unknown. We applied Gaussian band-pass filters to the 1146 and 1237 δ¹⁸O and δ¹³C series and the 1237 Fe series to extract oscillations associated with the 400 and 100 kyr periods. Gaussian bandpass filters were centered at 0.01 kyr⁻¹ (100 kyr period) with 0.003 kyr⁻¹ bandwidth (76.9–142.9 kyr period) and 0.0025 kyr⁻¹ (400 kyr period) with 0.0005 kyr⁻¹ bandwidth (333.3–500.0 kyr period). Orbital tuning, bandpass-filtering and sedimentation rates calculation were performed with AnalySeries 1.2 (Paillard et al., 1996).

2.4. XRF scanning

We performed X-ray fluorescence measurements with 1 cm resolution (~1–2 kyr time resolution) on the archive halves of the Site 1237 splice using the XRF Core Scanner at the Bremen IODP Core Repository. We interpreted Fe maxima as intervals of increased carbonate dissolution caused by poor deep water ventilation and not as intervals of increased terrigenous dust flux or river runoff, based on the co-variance between Fe and Mg, and the lack of co-variance between Fe and Ti (Holbourn et al., 2005). Data sets are archived at WDC-MARE (<http://www.pangaea.de>).

2.5. Spectral and time-frequency analysis

Cross spectra of benthic foraminiferal δ¹³C, δ¹⁸O (1237 and 1146), XRF Fe, fraction >63 μm (1237) with eccentricity–tilt (ET) tuning target were estimated using SPECTRUM (Schulz and Stattegger, 1997; available from www.palmod.uni-bremen.de/~mschulz) with 6 segments, a Hanning window, and an oversampling factor of 8.

Temporal changes in amplitude of signal components in the Milankovitch band were estimated using a modified harmonic-filtering algorithm (Ferraz-Mello, 1981), which fits sinusoidal waves to a time series by means of

least-squares. This method can process unevenly spaced time series directly, that is, without the requirement of prior interpolation. To obtain time-dependent amplitude estimates, the input time series is analyzed within a moving window of width $T_w = w \times T_f$, where $w=4$ is a width-factor and T_f denotes the signal periodicity of interest (e.g. 400 kyr). The window is shifted consecutively by one data point along the time axis of the input time series. Each “window segment” is linearly detrended prior to tapering with a Welch-Shape-1 window (Welch, 1967). The resulting amplitude and phase of the best-fit sinusoid are saved vs. the average of the observation times within the current segment and are used to reconstruct the signal component as function of time. The result of this procedure is equivalent to band-pass filtering (cf. Hinno et al., 2002). The selected value of w offers a good compromise between statistical and systematic errors and results in a half-amplitude bandwidth of approximately $0.5/T_f$ cycles/Myr. Note that due to the finite window width, a step-like increase in signal amplitude appears $w \times T_f$ wide. Applying the above filtering algorithm over a predefined range of frequencies allows us to detect changes in signal components in time-frequency space (Schulz et al., 1999). The dependence of window width, T_w on frequency leads to a change in temporal resolution with frequency. At low (high) frequencies wide (narrow) windows result in a low (high) temporal resolution. This scale dependence of the temporal resolution is similar to that of wavelet analysis. A program for time-frequency analysis (TIMEFRQ, version 4.3) is available from www.palmod.uni-bremen.de/~mschulz.

3. Results

3.1. Middle Miocene astronomically-tuned chronology

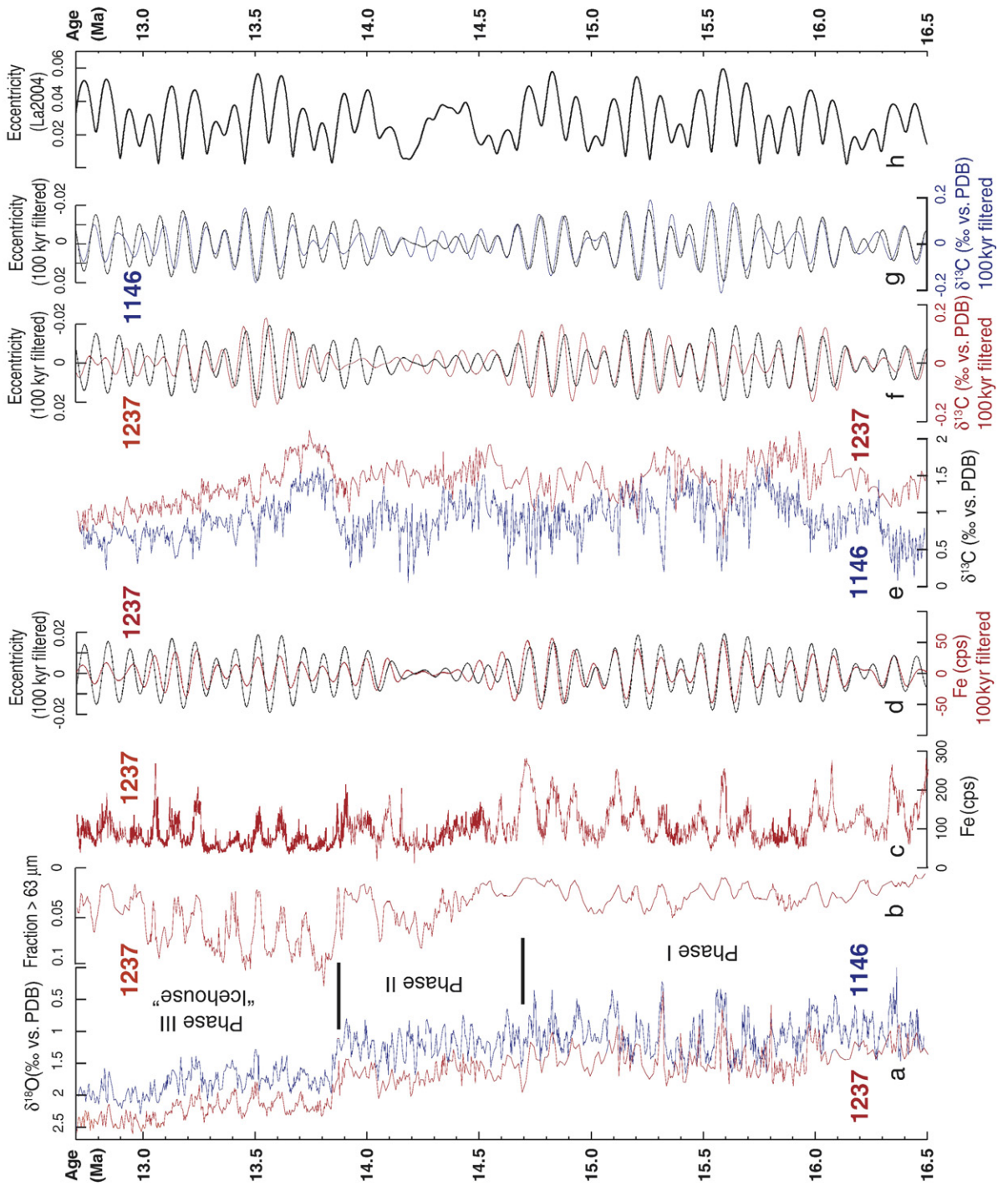
For Site 1146, we used the revised shorebased planktonic foraminiferal and nannofossil biostratigraphy from Nathan and Leckie (2003) with updated ages from ATNTS2004 (Lourens et al., 2004). We also revised the 1237 shipboard biostratigraphy, based on higher resolution sampling, then integrated data derived from stacked shipboard inclination data between 197 and 208 mcd, following ages in ATNTS2004. The 1146 and 1237 age

models are constrained by 15 biostratigraphic data (Supplementary Table 1) and by 10 magnetostratigraphic and 8 biostratigraphic data, respectively (Supplementary Table 2). These revised age models provided the framework to generate astronomically-tuned chronologies over the interval 12.7–16.5 Ma in Site 1146 and over the interval 12.7–17.1 Ma in Site 1237, thus extending the tuning of the 12.7–14.7 Ma intervals published earlier (Holbourn et al., 2005). The 1146 and 1237 benthic foraminiferal stable isotope data sets are plotted against composite depth in Supplementary Fig. 1 and against age in Figs. 2,3. Age tiepoints between $\delta^{18}\text{O}$ and ET series are shown in Figs. 2,3 and Supplementary Table 3. We note that the short eccentricity (100 kyr) and obliquity (41 kyr) periods are prominent in the untuned $\delta^{18}\text{O}$ records, and the amplitude modulation of these two periods is consistent with the astronomical target curve. In particular, the low amplitude of short eccentricity between 14.2 and 14.6 Ma is clearly reflected in the 1146 $\delta^{18}\text{O}$ data, which predominantly exhibit 41 kyr variability during this interval (Figs. 2,4,5).

The average sedimentation rate in Site 1146 is ~ 3 cm kyr^{-1} with a chronologic resolution of ~ 4 kyr for the stable isotope time series. The average sedimentation rate in Site 1237 is ~ 1 cm kyr^{-1} with a chronologic resolution of ~ 4 –9 kyr (Supplementary Figs. 2,3). The change in sedimentation rate at ~ 216 mcd in Site 1237 is supported by XRF Fe and coarse fraction (>63 μm) data, indicating a corresponding increase in carbonate dissolution (Fig. 4; Holbourn et al., 2005). Comparison of datum ages in ATNTS2004 with ages derived from astronomically-tuned age models developed here shows a reasonably good match, taking into account uncertainties related to biogeographic distribution, taxonomic concept, preservational bias, placement of data depth within cores, temporal resolution of orbital tuning and for data older than 13 Ma the lack of direct astronomical calibration in ATNTS2004.

We additionally revised the chronology of middle Miocene isotopic records from southwestern Pacific Site 588 and Southern Ocean Site 1171 (Flower and Kennett, 1993; Shevenell and Kennett, 2004; Shevenell et al., 2004) in order to enable valid comparisons with our records. To this end, we correlated the 588 and 1171 benthic foraminiferal $\delta^{18}\text{O}$ profiles to the 1146 and 1237

Fig. 4. Paleoceanographic records from ODP Sites 1146 and 1237: (a) Benthic foraminiferal $\delta^{18}\text{O}$. (b) 1237 proportion of coarse fraction >63 μm . (c) 1237 iron content in counts per second (cps). (d) Comparison of 100 kyr filtered 1237 $\delta^{18}\text{O}$ (red) and eccentricity from La2004 (black). (e) Benthic foraminiferal $\delta^{13}\text{C}$. (f) Comparison of 100 kyr filtered 1237 $\delta^{13}\text{C}$ (red) and eccentricity from La2004 (black). (g) Comparison of 100 kyr filtered 1146 $\delta^{13}\text{C}$ (blue) and eccentricity from La2004 (black). (h) Eccentricity from Laskar et al. (2004). (For interpretation of the references to colour in this figure legend, the reader is referred to the web version of this article.)



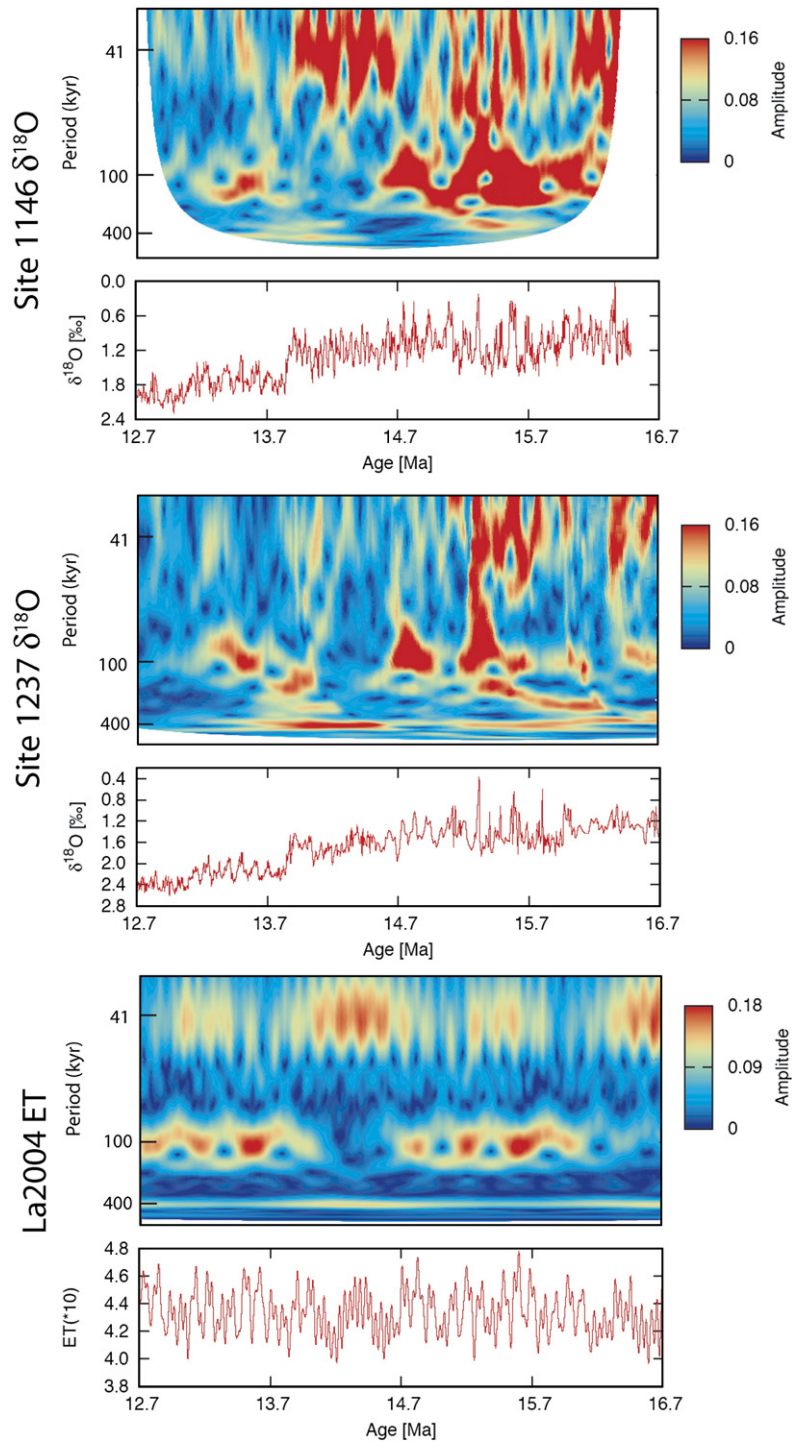


Fig. 5. Signal evolution in time-frequency space of eccentricity–tilt (ET) tuning target from [Laskar et al. \(2004\)](#) and of $\delta^{18}\text{O}$ in ODP Sites 1146 and 1237. The 100 and 41 kyr signal components in $\delta^{18}\text{O}$ show amplitude evolution similar to that of eccentricity and obliquity. Deep-water cooling and Antarctic ice-sheet expansion coincided with a transition from high amplitude in the 41 kyr band to high amplitude in the 100 kyr band. Signal amplitudes are in same units as data analyzed.

$\delta^{18}\text{O}$ time series, using the age tie points shown in Supplementary Table 4. Following this tuning procedure, we noted that the 588 and 1171 $\delta^{13}\text{C}$ curves also showed a reasonably good match with the 1146 and 1237 $\delta^{13}\text{C}$ profiles, thus supporting the revised 588 and 1171 age models derived from correlation of $\delta^{18}\text{O}$.

3.2. Orbital modulation of $\delta^{18}\text{O}$, $\delta^{13}\text{C}$ and carbonate dissolution proxies

The $\delta^{13}\text{C}$ and $\delta^{18}\text{O}$ time series are characterized by high-frequency (100 kyr) variations that closely follow the amplitude modulation of the short eccentricity period and are superposed on lower frequency (400 kyr) oscillations (Figs. 2–6). Comparison of 100 kyr filtered $\delta^{13}\text{C}$ and $\delta^{18}\text{O}$ data shows that the two signals co-vary, although the amplitude of 100 kyr oscillations is generally higher at the shallower northwestern Pacific Site 1146, especially prior to 14.7 Ma. A striking feature of the $\delta^{18}\text{O}$ time series is the major increase at 13.91–13.84 Ma (0.8‰ in Site 1237 and 1.2‰ in Site 1146), widely associated with Antarctic ice sheet expansion. In contrast to $\delta^{13}\text{C}$, the 1146 and 1237 $\delta^{18}\text{O}$ signals also show significant power in the 41 kyr band and high coherency (above 95% significance level) at the 41 kyr obliquity period (Figs. 5–7, Supplementary Figs. 4,5).

The 1.2 Myr amplitude modulation of the obliquity cycle is clearly imprinted in the 1146 $\delta^{18}\text{O}$ signal, although it is less obvious in the 1237 $\delta^{18}\text{O}$ series (Fig. 5; Supplementary Fig. 4), which may be due to the lower sedimentation rates in this site.

The 400 and 100 kyr rhythm is also prominent in proxy records of carbonate dissolution (XRF Fe and coarse fraction $>63\ \mu\text{m}$) in the deeper southeastern Pacific Site 1237, located in paleodepths close to the lysocline (Fig. 4, Supplementary Fig. 5). Cross-spectral analysis with ET indicates significant coherency ($\alpha=0.05$) at periods of 100 and 400 kyr for the 1237 $\delta^{18}\text{O}$, $\delta^{13}\text{C}$, XRF Fe and fraction $>63\ \mu\text{m}$ (Fig. 7, Supplementary Fig. 5). Positive phase angle in the 400 kyr band for $\delta^{13}\text{C}$ in Site 1237 indicates that positive ET values lead negative $\delta^{13}\text{C}$ excursions by a minimum of $42\pm 20^\circ$ or 47 ± 18 kyr (95% confidence interval). Cross-spectral analysis of $\delta^{18}\text{O}$ and $\delta^{13}\text{C}$ in Site 1237 also supports a lag of the carbon cycle over climate changes at both these eccentricity periods (Supplementary Fig. 5). However in the shallower northwestern Pacific Site 1146, coherency of $\delta^{13}\text{C}$ with long eccentricity is below the 95% significance level and cross-spectral analysis of $\delta^{18}\text{O}$ and $\delta^{13}\text{C}$ reveals no significant phase lag at the 100 and 400 kyr periods, whereas coherency with short eccentricity is significant for both

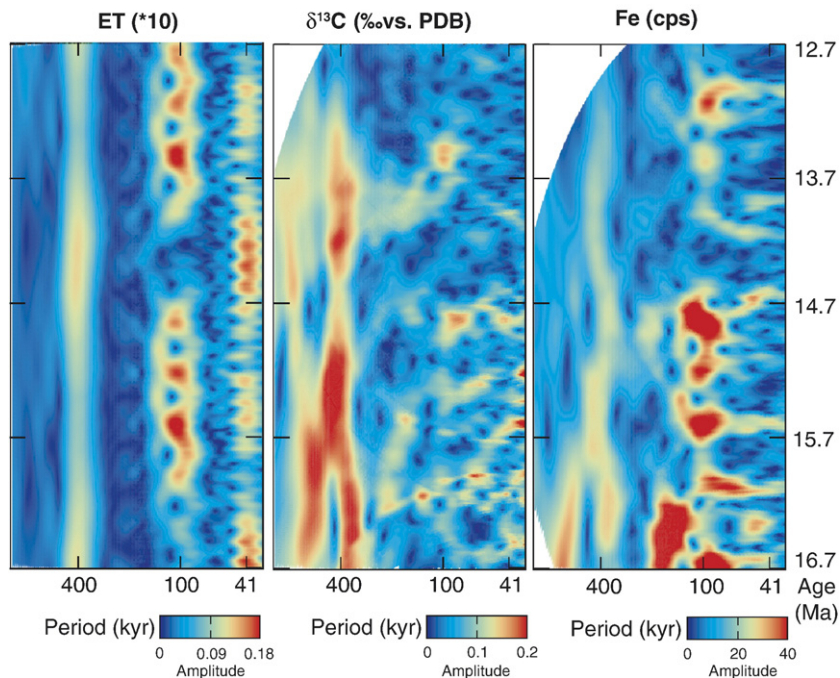


Fig. 6. Signal evolution in time-frequency space of eccentricity–tilt (ET) tuning target (from Laskar et al., 2004), Fe and $\delta^{13}\text{C}$ in ODP Site 1237. Fe signal shows similar amplitude evolution as the short and long eccentricity periods, whereas $\delta^{13}\text{C}$ signal follows mainly the long eccentricity. Signal amplitudes are in same units as data analyzed.

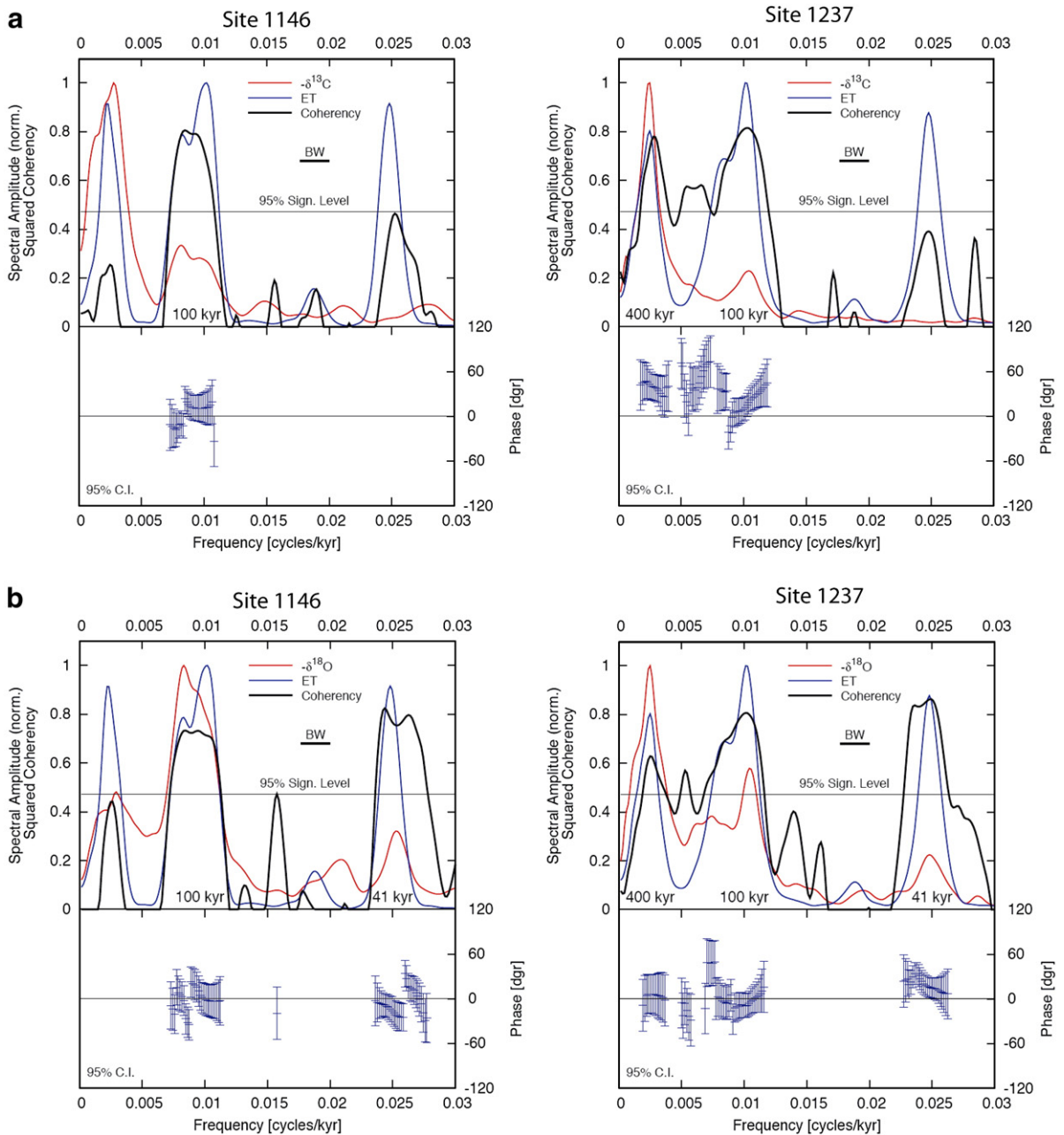


Fig. 7. (a–b). a Top: Normalized power spectra of negative 1146 $\delta^{13}\text{C}$, negative 1237 $\delta^{13}\text{C}$ and ET tuning target as well as squared coherency between both series. a Bottom: Phase spectrum between $\delta^{13}\text{C}$ (inverted) and ET series. Positive values indicate a lead of ET over $\delta^{13}\text{C}$. 95% confidence intervals are only shown if the coherency is significant ($\alpha=0.05$; horizontal line indicates false alarm level for coherency). Horizontal bar indicates 6-dB bandwidth. Numbers below peaks indicate associated periods in kyr. b: as Fig. 6a but for negative 1146 $\delta^{18}\text{O}$, negative 1237 $\delta^{18}\text{O}$ and ET tuning target.

$\delta^{18}\text{O}$ and $\delta^{13}\text{C}$ (Fig. 7, Supplementary Fig. 5). Discrepancies between spectral characteristics in Sites 1146 and 1237 may be explained by the fact that marked negative deviations in 1146 $\delta^{13}\text{C}$ (up to $\sim 1\text{‰}$) occur at $\sim 16.5\text{--}16.4$, $16.1\text{--}15.9$, $15.3\text{--}15.2$ and $14.3\text{--}14.1$ Ma, whereas the 1146 and 1237 $\delta^{13}\text{C}$ series are significantly

coherent ($\alpha=0.05$, not shown) over the interval 12.7 to 13.9 Ma, showing an offset of $\sim 0.5\text{‰}$ with lower 1146 values (Fig. 4).

Although the beginning of the ‘‘Monterey Excursion’’ is not captured in the 1146 $\delta^{13}\text{C}$ record, which only reaches down to 16.5 Ma (Fig. 2), a first $\delta^{13}\text{C}$ maximum

>1.4‰ (CM1) is clearly recorded at ~16.8 Ma (234 mcd) in the more extended 1237 $\delta^{13}\text{C}$ series (Fig. 3; Supplementary Fig. 1). An age of ~16.8 Ma for the earliest $\delta^{13}\text{C}$ maxima in the “Monterey Excursion” was also suggested from astronomically tuned $\delta^{13}\text{C}$ stratigraphy in Site 929 (Flower et al., 1997; Shackleton et al., 1999). Therefore based on the 1237 record, the “Monterey Excursion” consists of nine successive 400 kyr cycles between 16.9 and 13.5 Ma (Fig. 3), in contrast to the original six carbon-isotope maxima initially identified by Woodruff and Savin (1991) within this interval. Our data indicate that CM3, CM4 and CM5 include each two 400 kyr cycles instead of a single cycle, as originally suggested by Woodruff and Savin (1991). This discrepancy probably arises from the fact that most of the records examined by these authors were of comparatively lower stratigraphic resolution and/or afflicted by stratigraphic gaps due to diagenetic overprints and carbonate dissolution, particularly within the earlier part of the “Monterey Excursion”. The younger carbon-isotope maximum (CM7) recognized at 11.5 Ma by Woodruff and Savin (1991) lies beyond the interval covered by our data sets.

4. Discussion

4.1. Middle Miocene long-term climate evolution

We recognize three distinct climate phases with typical amplitude variations and different imprints of orbital variations into the climatic signals (Fig. 3). Phase 1, broadly corresponding to the climate optimum (prior to 14.7 Ma), is characterized by high-amplitude 100 kyr variability in $\delta^{18}\text{O}$ and by prominent 400 kyr oscillations in $\delta^{13}\text{C}$ that follow Earth’s long eccentricity. Peak minimum values in benthic foraminiferal $\delta^{18}\text{O}$ and in the proportion of 1237 coarse fraction >63 μm are reached in Site 1237 during this interval, pointing to minimum ice volume and to poor ventilation in the deep southeastern Pacific. During Phase 2 (~14.7 to 13.9 Ma), a long-term trend towards heavier $\delta^{18}\text{O}$ values modulated by obliquity, indicates punctuated climate cooling. During this transitional phase, $\delta^{13}\text{C}$ continues to show high-amplitude 400 kyr variability and the $\delta^{13}\text{C}$ gradient between Sites 1146 and 1237 intensifies. Coarse fraction values in Site 1237 indicate a transient improvement in southeastern Pacific deep-water ventilation. Phase 2 culminates with the massive stepped increase in $\delta^{18}\text{O}$ at 13.87–13.84 Ma, marking entry into the “Icehouse”. During Phase 3 (after 13.9 Ma), $\delta^{18}\text{O}$ exhibits a long-term increasing trend and prominent variability at the 100 kyr band. $\delta^{13}\text{C}$ initially displays the highest values

of the whole middle Miocene at 13.8–13.6 Ma (CM6), but subsequently shows reduced amplitude variations and long-term declining values. During this eccentricity-paced glacial–interglacial climate mode, the $\delta^{13}\text{C}$ gradient between Sites 1146 and 1237 remains relatively consistent (~0.4‰).

The initiation of new climatic phases appears to coincide with marked changes in Earth’s orbital rhythm (Figs. 4–6). The transition from Phase 1 to 2 corresponds to a change from high to low eccentricity fluctuations with concurrent increase in obliquity variability. The transition into Phase 3 occurs more abruptly at the start of an obliquity node, also marking the onset of a period with low eccentricity. This congruence supports the suggestion that low seasonality at obliquity nodes in combination with eccentricity minima at 400 kyr and 2.4 Myr interval induced high latitude cooling and ice sheet expansion in the Paleogene and early Neogene due to inhibition of summer ice melting (Zachos et al., 2001b; Wade and Pälike, 2004; Abels et al., 2005; Pälike et al., 2006). However during the middle Miocene, the 1.2 Myr modulation of the obliquity cycle is not invariably associated with global cooling and ice growth events. For instance, the 1146 and 1237 $\delta^{18}\text{O}$ records indicate no major ice expansion during concurrent obliquity and eccentricity minima at ~16.2 Ma, although a substantial increase in $\delta^{13}\text{C}$ occurred (Fig. 4). This implies that the middle Miocene climate response was not solely coupled to changing high-latitude insolation and that additional interactions and/or feedback mechanisms such as tectonic events, circulation patterns, ice-sheet dynamics played a role in controlling long-term climate evolution.

4.2. Middle Miocene Pacific circulation

A remarkable feature in the deeper Site 1237, located in paleodepths close to the lysocline in the southeastern Pacific, is the occurrence of eccentricity-paced carbonate dissolution cycles during warmer intervals, as revealed by the co-variance between $\delta^{18}\text{O}$, Fe and coarse fraction data (Fig. 4). These patterns bear similarity to late Pleistocene dissolution cycles in the Pacific, which occurred in anti-phase to Atlantic cycles (Crowley, 1985; Farrell and Prell, 1991; Le and Shackleton, 1992). This phase difference between the two oceans was related to variable production of North Atlantic deep-water during glacial and interglacial periods (Boyle and Keigwin, 1985). During glacials, less corrosive bottom waters filled the Pacific following changes in intermediate- and deep-water production. Although the same scenario is unlikely during the middle Miocene, when

global ice volume and the configuration of oceanic gateways substantially differed, a comparable glacial–interglacial switch in deep-water sourcing evidently occurred on a 100 kyr timescale. Enhanced carbonate dissolution during middle Miocene warm phases may have stemmed from reduced production of well-ventilated Southern Ocean deep-water and increased influence of corrosive “old” deep-water from a northern source. The XRF Fe and coarse fraction data from the deeper Site 1237 further reveal enhanced carbonate preservation after 13.9 Ma in particular during cold phases (Fig. 4), indicating that global cooling and ice-sheet expansion were associated with a substantial improvement in deep-water ventilation and a re-organization in Pacific circulation.

Interestingly, the $\delta^{13}\text{C}$ records from Site 1171 (Tasman Rise, 2 147.8 m water depth; Shevenell and Kennett, 2004) and Site 588 (southwestern Pacific, 1 533 m water depth; Flower and Kennett, 1993) are virtually identical with the 1237 $\delta^{13}\text{C}$ signal over the whole middle Miocene (Fig. 8), indicating a relatively homogenous deep-water mass in the South Pacific, which extended from the northern sector of the Southern Ocean. In contrast, $\delta^{13}\text{C}$ values are markedly lower in Site 1146 with pronounced deviations at ~ 16.5 – 16.4 , 16.1 – 15.9 , 15.3 – 15.2 and 14.3 – 14.1 Ma, suggesting that northern source intermediate-water was more influential at this marginal, northwestern Pacific location, especially during the warmer climatic phases preceding ice expansion. Prevalence of North Pacific sources would have sporadically resulted in water masses with different hydrographic properties in Site 1146. Alternatively, the 1146 $\delta^{13}\text{C}$ signal may also carry a strong imprint of regional paleoproductivity patterns, in contrast to the signal in the more pelagic Site 1237.

The marked hydrographic asymmetry between the North and South Pacific is somewhat reminiscent of present day deep and intermediate water mass distribution with low $\delta^{13}\text{C}$ (poorly ventilated, nutrient-rich) waters in the North contrasting with high $\delta^{13}\text{C}$ (well-oxygenated, nutrient-poor waters) in the South, as shown by a comparison of modern deep Pacific circulation with $\delta^{13}\text{C}$ peak values at ~ 13.8 Ma during CM6 (Fig. 9). However, the source and chemistry of middle Miocene water masses must have significantly differed as the Central American Seaway was widely open and deep-water connections to the Tethys may have also existed. Interestingly, the 1237 $\delta^{13}\text{C}$ signal shows high coherency with long eccentricity, whereas coherency is below 95% significance in 1146 (Fig. 7). Thus, the 1237 $\delta^{13}\text{C}$ curve is probably more representative of the global $\delta^{13}\text{C}$ signal (reflecting carbon

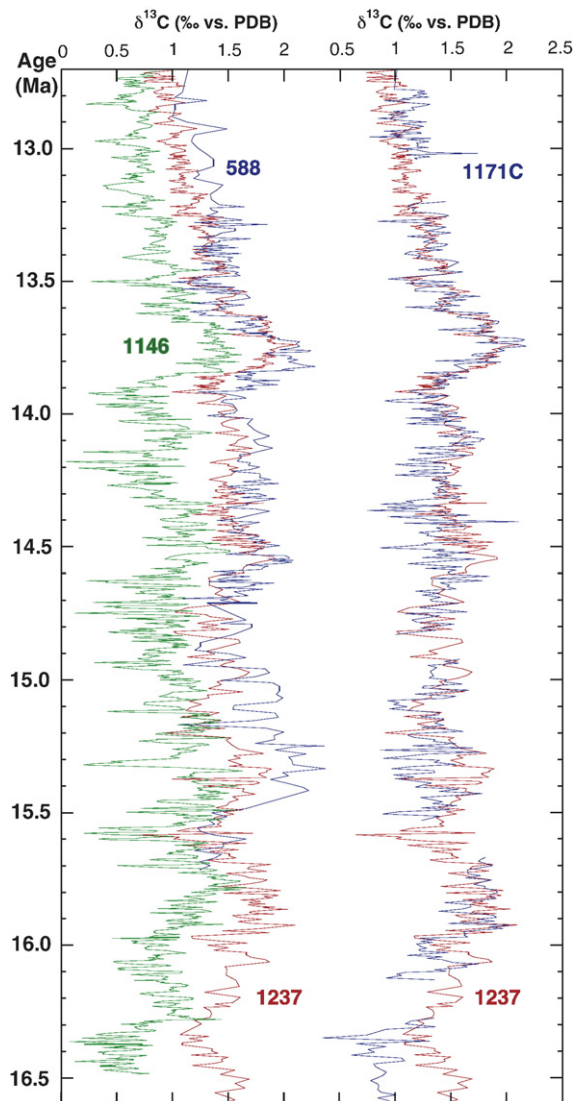


Fig. 8. Comparison of benthic foraminiferal $\delta^{13}\text{C}$ in DSDP Site 588, ODP Sites 1146, 1171 and 1237 reveals a relatively homogenous deep-water mass in the South Pacific (Sites 588, 1171 and 1237) during the middle Miocene. Site 588 isotopic data from Flower and Kennett (1993), Site 1171 isotopic data from Shevenell and Kennett (2004).

reservoir changes), because this site was relatively close to the locus of deep-water formation in the Southern Ocean, which also played a crucial role in the transmission of global climate change during the middle Miocene.

4.3. Ocean–atmosphere carbon transfer and climate change

The global nature of the “Monterey” $\delta^{13}\text{C}$ excursion, evident in marine isotope records including benthic and

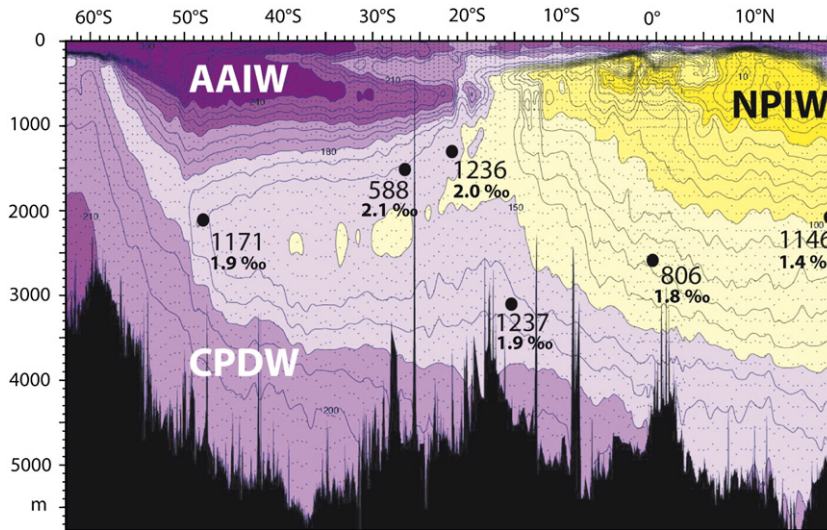


Fig. 9. Present-day Pacific dissolved O_2 and water mass distribution from Woce Pacific Ocean Atlas. Also shown are middle Miocene peak $\delta^{13}C$ values during last and most pronounced $\delta^{13}C$ increase (CM6). Site 588 $\delta^{13}C$ from Flower and Kennett (1993), Site 1171 $\delta^{13}C$ from Shevenell and Kennett (2004), Sites 806 and 1236 $\delta^{13}C$ from Holbourn et al. (unpublished data). A marked hydrographic asymmetry prevailed in the Pacific during the middle Miocene with poorly ventilated, nutrient-rich waters (low $\delta^{13}C$) in the North contrasting with well-oxygenated, nutrient-poor waters (high $\delta^{13}C$) in the South.

planktonic foraminiferal and bulk carbonate records, implies carbon reservoir changes linked to eccentricity forcing, possibly mediated through enhanced biological productivity and increased organic carbon burial in continental margin sediments (Woodruff and Savin, 1991; Flower and Kennett, 1993, 1994; Shevenell and Kennett, 2004; Katz et al., 2005). The distinctive eccentricity rhythm during the “Monterey” excursion may have stemmed from enhanced organic carbon burial at low eccentricity, favoring atmospheric CO_2 drawdown and global cooling, when insolation variations were minimal and the ocean–climate system more susceptible to CO_2 changes (Berger and Loutre, 2003). Conversely at high eccentricity, the strong variability in precessional insolation may have induced higher carbonate production in tropical shallow seas through enhanced monsoons during insolation maxima and a decreased capacity of the deep ocean to store carbonate, resulting in an overall depletion in ^{13}C in the marine carbon reservoir and net release of CO_2 to the atmosphere.

The benthic foraminiferal $\delta^{13}C$ record in Site 1237 shows significant coherence ($\alpha=0.05$) with the 400 kyr eccentricity cycle between 17.1 and 13.2 Ma, when eccentricity maxima correspond to low $\delta^{13}C$ and eccentricity minima coincide with high $\delta^{13}C$ (Figs. 3,7). In contrast to carbonate dissolution proxies, which are in phase with eccentricity at both the 100 and 400 kyr bands, $\delta^{13}C$ exhibits a $\sim 50\pm 20$ kyr phase lag (95% confidence interval) to maximum eccentricity at the

400 kyr band but shows no significant phasing in the 100 kyr band (Figs. 3,7). A similar phase relationship between $\delta^{13}C$ and the long eccentricity period was detected in older climate modes of the Cenozoic (Zachos et al., 2001a; Wade and Pälike, 2004; Pälike et al., 2006). Both the 100 and 400 kyr signals must be related to changes in the Pacific carbon cycle, but the unusual long phase lag of 50 ± 20 kyr in the 400 kyr band compared to the near-zero phase offset at 100 kyr poses a challenge.

Simple linear models of the global carbon cycle, which would have some inertia to react to orbital forcing would result in exactly the opposite phase behavior, that is, the lag between $\delta^{13}C$ and eccentricity would rise with increasing frequency (e.g., Imbrie, 1985). Recent modeling studies related the prominent 400 kyr cyclicity in marine $\delta^{13}C$ to an amplification of longer forcing periods due to the long residence time of carbon in the ocean (~ 100 kyr, Broecker and Peng, 1982) in combination with a dampening effect of deep-sea sedimentary carbonate redissolution on the shorter term forcing (Pälike et al., 2006). A plausible mechanism would invoke enhanced and delayed response of continental weathering to orbital forcing at the 400 kyr period, compared to the 100 kyr band, due to the long timescale associated with weathering. If the marine carbon cycle responds otherwise “fast” to orbital forcing, imprinting the delayed and low-pass filtered weathering signal onto the marine carbon cycle via global runoff could potentially result in the estimated

phase behavior. Pälike et al. (2006) additionally suggested that the different phase lag of $\delta^{13}\text{C}$ with long and short eccentricity may in part be explained by the transfer of energy from the precessional into the eccentricity bands, resulting in a frequency dependent phase lag of $\delta^{13}\text{C}$. This relationship between positive carbon-isotope excursions, long-term global carbon budgets and eccentricity appears not to be unique for the middle Miocene. Eccentricity forcing was probably a prime pacemaker of climate evolution over the past 100 Ma through the modulation of circulation patterns, carbonate production and organic carbon burial processes (cf. Shackleton, 1977, 2000).

5. Conclusion

Orbitally-tuned climate proxy records in ODP Site 1146 (northwestern Pacific) and ODP Site 1237 (southwestern Pacific) provide new insights into the Miocene “Monterey” carbon-isotope excursion and associated climatic transition. The extended 1237 record reveals that the “Monterey Excursion” consists of nine successive 400 kyr $\delta^{13}\text{C}$ cycles between 16.9 and 13.5 Ma, in contrast to the original six carbon-isotope maxima identified by Woodruff and Savin (1991). Superposed on low-frequency $\delta^{18}\text{O}$ and $\delta^{13}\text{C}$ fluctuations are high-frequency (100 kyr) variations that closely track the amplitude modulation of the short eccentricity period in both sites. The 1146 and 1237 $\delta^{18}\text{O}$ signals additionally show significant power in the 41 kyr band and the 1.2 Myr amplitude modulation of the obliquity cycle is clearly imprinted in the 1146 $\delta^{18}\text{O}$ signal. Low seasonality at high latitudes during obliquity and eccentricity minima appears instrumental in triggering rapid ice growth and global cooling after 13.9 Ma (Holbourn et al., 2005), although additional forcing factors must have also controlled long-term climate evolution.

We recognize three distinct climate phases with different imprints of orbital variations into the climate proxy signals (1146 and 1237 $\delta^{18}\text{O}$, $\delta^{13}\text{C}$; 1237 XRF Fe, fraction $>63\ \mu\text{m}$): (1) climate optimum prior to 14.7 Ma characterized by minimum ice volume and prominent 100 and 400 kyr variability, (2) long-term cooling primarily modulated by obliquity from 14.7 to 13.9 Ma, which ended with rapid ice growth and global cooling at the onset of the last and most pronounced $\delta^{13}\text{C}$ increase, (3) “Icehouse” mode after 13.9 Ma with a distinct 100 kyr rhythm in climate and circulation patterns. Final entry into the “Icehouse” culminated with a substantial improvement in deep-water ventilation and intensified production of southern source deep and intermediate waters.

Acknowledgements

We thank the Co-chiefs and Shipboard Scientific Parties of ODP Legs 184 and 202 for their dedication and efforts, A. Coe, F. Hilgen and L. Lourens for their constructive comments on an earlier version of the manuscript, U. Röhl and colleagues at Bremen University for their valuable advice regarding XRF scanning. Our manuscript benefited considerably from indepth reviews by B. Flower, P. Delaney and an anonymous reviewer. This research used samples provided by the Integrated Ocean Drilling Program (IODP), and was funded by the Deutsche Forschungsgemeinschaft.

Appendix A. Supplementary data

Supplementary data associated with this article can be found, in the online version, at [doi:10.1016/j.epsl.2007.07.026](https://doi.org/10.1016/j.epsl.2007.07.026).

References

- Abels, H.A., Hilgen, F.J., Krijgsman, W., Kruk, R.W., Raffi, I., Turco, E., Zachariasse, W.J., 2005. Long-period orbital control on middle Miocene global cooling: integrated stratigraphy and astronomical tuning of the Blue Clay Formation on Malta. *Paleoceanography* 20. doi:10.1029/2004PA001129.
- Berger, A., Loutre, M.-F., 2003. Climate 400,000 years ago, a key to the future. In: Droxler, A.W., Poore, R.Z., Burckle, L.H. (Eds.), *Earth's Climate and Orbital Eccentricity: the Marine Isotope Stage 11 Question*. Geophysical Monograph Series, vol. 137. American Geophysical Union, Washington, DC, pp. 17–26.
- Boyle, E.A., Keigwin, L.D., 1985. Comparison of Atlantic and Pacific paleochemical records for the last 215,000 years: changes in deep ocean ventilation and chemical inventories. *Earth Planet. Sci. Lett.* 76, 135–150.
- Broecker, W.S., Peng, T.H., 1982. *Tracers in the Sea*. Eldigio Press Lamont Doherty Geological Observatory, p. 690.
- Clemens, S., 1999. An astronomical tuning strategy for Pliocene sections: implications for global-scale correlation and phase relationships. *Philos. Trans. R. Soc. Lond., A Contain. Pap. Math. Phys. Character* 357, 1949–1973.
- Crowley, T.J., 1985. Late Quaternary carbonate changes in the North Atlantic and Atlantic/Pacific comparison. In: Sundquist, E.T., Broecker, W.S. (Eds.), *The Carbon Cycle and Atmospheric CO₂: Natural Variations Archean to Present*. Geophysical Monograph Series, vol. 32. American Geophysical Union, Washington, DC, pp. 271–284.
- Farrell, J.W., Prell, W.L., 1991. Pacific CaCO₃ preservation and $\delta^{18}\text{O}$ since 4 Ma: paleoceanic and paleoclimatic implications. *Paleoceanography* 6, 485–498.
- Ferraz-Mello, S., 1981. Estimation of periods from unequally spaced observations. *Astron. J.* 86, 619–624.
- Flower, B.P., Kennett, J.P., 1993. Middle Miocene ocean–climate transition: high resolution oxygen and carbon isotopic records from DSDP Site 588A, southwest Pacific. *Paleoceanography* 8, 811–843.
- Flower, B.P., Kennett, J.P., 1994. The middle Miocene climatic transition: East Antarctic ice sheet development, deep ocean

- circulation and global carbon cycling. *Palaeogeogr. Palaeoclimatol. Palaeoecol.* 108, 537–555.
- Flower, B.P., Zachos, J.C., Martin, E., 1997. Latest Oligocene through Early Miocene isotopic stratigraphy and deepwater paleoceanography of the Western Equatorial Atlantic: sites 926 and 929. In: Shackleton, N.J., Curry, W.B., Richter, C., Bralower, T.J. (Eds.), *Proceedings of the Ocean Drilling Program, Scientific Results*, vol. 154. Ocean Drilling Program, College Station, TX, pp. 451–461.
- Hilgen, F.J., Krijgsman, W., Langereis, C.G., Lourens, L.J., Santarelli, A., Zachariasse, W.J., 1995. Extending the astronomical (polarity) time scale into the Miocene. *Earth Planet. Sci. Lett.* 136, 495–510.
- Hilgen, F.J., Bissoli, L., Iaccarino, S., Krijgsman, W., Meijer, R., Negri, A., Villa, G., 2000. Integrated stratigraphy and astrochronology of the Messinian GSSP at Qued Akrech (Atlantic Morocco). *Earth Planet. Sci. Lett.* 182, 237–251.
- Hilgen, F.J., Abdul Aziz, H., Krijgsman, W., Raffi, I., Turco, E., 2003. Integrated stratigraphy and astronomical tuning of the Serravalian and lower Tortonian at Monte dei Corvi (Middle–Upper Miocene, northern Italy). *Palaeogeogr. Palaeoclimatol. Palaeoecol.* 199, 229–264.
- Hinnov, L.A., Schulz, M., Yiou, P., 2002. Interhemispheric space–time attributes of the Dansgaard-Oeschger oscillations between 100 and 0 ka. *Quat. Sci. Rev.* 21, 1213–1228.
- Holbourn, A.E., Kuhnt, W., Schulz, M., Erlenkeuser, H., 2005. Impacts of orbital forcing and atmospheric CO₂ on Miocene ice-sheet expansion. *Nature* 438, 483–487.
- Hüsing, S.K., Hilgen, F.J., Abdul Aziz, H., Krijgsman, W., 2007. Completing the Neogene geological time scale between 8.5 and 12.5 Ma. *Earth Planet. Sci. Lett.* 253, 340–358.
- Imbrie, J., 1985. A theoretical framework for the Pleistocene ice ages. *J. Geol. Soc. (Lond.)* 142, 417–432.
- Imbrie, J., Hays, J.D., Martinson, D.G., McIntyre, A., Mix, A.C., Morley, J.J., Pisias, N.G., Prell, W.L., Shackleton, N.J., 1984. The orbital theory of Pleistocene climate: support from a revised chronology of the marine $\delta^{18}\text{O}$ record. In: Berger, A.L., Imbrie, J., Hays, J., Kukla, G., Saltzman, B. (Eds.), *Milankovitch and Climate*, Part 1. D. Riedel, Hingham, MA, pp. 269–305.
- Katz, M.E., Wright, J.D., Miller, K.J., Cramer, B.S., Fennel, K., Falkowski, P.G., 2005. Biological overprint of the geological carbon cycle. *Mar. Geol.* 217, 323–338.
- Krijgsman, W., Hilgen, F.J., Raffi, I., Sierro, F.J., Wilson, D.S., 1999. Chronology, causes and progression of the Messinian salinity crisis. *Nature* 400, 655–662.
- Laskar, J., 1999. The limits of Earth orbital calculations for geological time-scale use. *Philos. Trans. R. Soc. Lond.* 357, 1735–1759.
- Laskar, J., Robutel, P., Joutel, F., Gastineau, M., Correia, A.C.M., Levrard, B., 2004. A long term numerical solution for the insolation quantities of the Earth. *Astron. Astrophys.* 428, 261–285.
- Le, J., Shackleton, N.J., 1992. Carbonate dissolution fluctuations in the Western Equatorial Pacific during the Late Quaternary. *Paleoceanography* 7, 21–42.
- Lourens, L., Hilgen, F., Shackleton, N.J., Laskar, J., Wilson, D., 2004. The Neogene period. In: Gradstein, F., Ogg, J., Smith, A. (Eds.), *A Geologic Time Scale*. Cambridge University Press, pp. 409–440.
- Miller, K.G., Wright, J.D., Fairbanks, R.G., 1991. Unlocking the ice house: Oligocene–Miocene oxygen isotopes, eustasy and margin erosion. *J. Geophys. Res.* 96, 6829–6848.
- Mix, A.C., Tiedemann, R., Blum, P., et al., 2003. Initial Reports, Ocean Drilling Program, Leg 202: College Station, Texas, Ocean Drilling Program [CD-ROM], available from: Ocean Drilling Program, Texas A&M University, College Station TX 77845-9547, USA.
- Muller, R.A., MacDonald, J., 2000. Ice ages and astronomical causes, data, spectral analysis and mechanisms. Springer Praxis Books in Environmental Sciences, p. 318.
- Nathan, S.A., Leckie, R.M., 2003. Miocene planktonic foraminiferal biostratigraphy of sites 1143 and 1146, ODP Leg 184, South China Sea. In: Prell, W.L., Wang, P., Blum, P., Rea, D.K., Clemens, S.C. (Eds.), *Scientific Results of the Ocean Drilling Program. Leg. vol. 184*. [Online] Available from World Wide Web: http://www-odp.tamu.edu/publications/184_SR/219/219.htm [Cited 2005-06-05].
- Pagani, M., Arthur, M.A., Freeman, K.H., 1999. Miocene evolution of atmospheric carbon dioxide. *Paleoceanography* 14, 273–292.
- Pagani, M., Lemarchand, D., Spivack, A., Gaillardet, J., 2005. A critical evaluation of the boron isotope–pH proxy: the accuracy of ancient oceans pH estimates. *Geochim. Cosmochim. Acta* 69, 953–961.
- Paillard, D., Labeyrie, L., Yiou, P., 1996. Macintosh program performs time-series analysis. *EOS Trans., Am. Geophys. Union* 77, 79.
- Pälike, H., Norris, R.D., Herrle, J.O., Wilson, P.A., Coxall, H.K., Lear, C.H., Shackleton, N.J., Tripathi, A.K., Wade, B.S., 2006. The heartbeat of the Oligocene climate system. *Science* 314, 1894–1998.
- Raymo, M.E., Nisancioglu, K., 2003. The 41 kyr world: Milankovitch’s other unsolved mystery. *Paleoceanography* 18, 1011. doi:10.1029/2002PA000791.
- Schulz, M., Statterger, K., 1997. SPECTRUM: spectral analysis of unevenly spaced paleoclimatic time series. *Comput. Geosci.* 23, 929–945.
- Schulz, M., Berger, W.H., Sarnthein, M., Grootes, P.M., 1999. Amplitude variations of 1470-year climate oscillations during the last 100,000 years linked to fluctuations of continental ice mass. *Geophys. Res. Lett.* 26, 3385–3388.
- Shackleton, N.J., 1977. Carbon-13 in *Uvigerina*: tropical rainforest history and the equatorial Pacific carbonate dissolution cycles. In: Andersen, N.R., Malahoff, A. (Eds.), *The Fate of Fossil Fuel CO₂ in the Oceans*. Plenum Press, pp. 401–427.
- Shackleton, N.J., 2000. The 100,000-year ice-age cycle identified and found to lag temperature, carbon dioxide, and orbital eccentricity. *Science* 289, 1897–1902.
- Shackleton, N.J., Crowhurst, S., 1997. Sediment fluxes based on an orbitally tuned time scale 5 Ma to 14 Ma, Site 926. In: Shackleton, N.J., Curry, W.B., Richter, C., Bralower, T.J., et al. (Eds.), *Proceedings of the Ocean Drilling Program, Scientific Results*, vol. 154. Ocean Drilling Program, College Station, TX, pp. 69–82.
- Shackleton, N.J., Hagelberg, T.K., Crowhurst, S.J., 1995. Evaluating the success of astronomical tuning: pitfalls of using coherence as a criterion for assessing pre-Pleistocene timescales. *Paleoceanography* 10, 693–697.
- Shackleton, N.J., Crowhurst, S.J., Weedon, G.P., Laskar, J., 1999. Astronomical calibration of Oligocene–Miocene time. *Philos. Trans. R. Soc. Lond.* 357, 1907–1929.
- Shevenell, A.E., Kennett, J.P., 2004. Paleoclimatological change during the middle Miocene climate revolution: an Antarctic stable isotope perspective. In: Exon, N., Kennett, J.P., Malone, M. (Eds.), *The Cenozoic Southern Ocean: Tectonics, Sedimentation and Climate Change between Australia and Antarctica*. Geophysical Monograph Series, vol. 151. American Geophysical Union, Washington, DC, pp. 235–252.
- Shevenell, A.E., Kennett, J.P., Lea, D.W., 2004. Middle Miocene Southern Ocean Cooling and Antarctic Cryosphere expansion. *Science* 305, 1766–1770.
- Vincent, E., Berger, W.H., 1985. Carbon dioxide and polar cooling in the Miocene: the Monterey hypothesis. In: Broecker, W.S., Sundquist, E.T. (Eds.), *The Carbon Cycle and Atmospheric CO₂: Natural Variations Archaean to Present*. Geophysical Monograph

- Series, vol. 32. American Geophysical Union, Washington, DC, pp. 455–468.
- Wade, B., Pälike, H., 2004. Oligocene climate dynamics. *Paleoceanography* 19. doi:10.1029/2004PA001042.
- Wang, P., Prell, W.L., Blum, P., et al., 2000. Initial Reports, Ocean Drilling Program, Leg 184: College Station, Texas, Ocean Drilling Program [CD-ROM], available from Ocean Drilling Program, Texas A&M University, College Station TX 77845-9547, USA.
- Welch, P.D., 1967. The use of fast Fourier transform for the estimation of power spectra: a method based on time averaging over short, modified periodograms. *IEEE Trans. Audio Electroacoust.* Au-15, 70–73.
- Woodruff, F., Savin, S., 1991. Mid-Miocene isotope stratigraphy in the deep sea: high resolution correlations, paleoclimatic cycles, and sediment preservation. *Paleoceanography* 6, 755–806.
- Zachos, J., Pagani, M., Sloan, L., Thomas, E., Billups, K., 2001a. Trends, rhythms, and aberrations in global climate 65 Ma to present. *Science* 292, 686–693.
- Zachos, J., Shackleton, N.J., Revenaugh, J.S., Pälike, H., Flower, B.P., 2001b. Climate response to orbital forcing across the Oligocene–Miocene boundary. *Science* 292, 274–278.